Journal of Materials Chemistry A

PAPER

View Article Online
View Journal

Cite this: DOI: 10.1039/c8ta10642h

Changes induced by transition metal oxides in Pt nanoparticles unveil the effects of electronic properties on oxygen reduction activity†

Felipe B. Ometto,[a] Emilia A. Carbonio,[b] Érico Teixeira-Neto ‡[c] and Hebe M. Villullas *[a]

Although the relevance of electronic effects in the electrocatalysis of the oxygen reduction reaction has been recognized, the impossibility of separating the effects of composition and particle size for Pt-based materials has hindered establishing clear activity–property relationships. Herein, we report a systematic study based on induced changes *via* the interactions of pure Pt nanoparticles with transition metal oxide/carbon supports (Pt/MO_x/C catalysts, MO_x = CeO_2, SnO_2, TiO_2, ZrO_2 and WO_3). A thorough analysis of aberration-corrected HR-STEM images demonstrated that Pt particles are similar in size and shape for all catalysts, while the direct probing of electronic properties by *in situ* X-ray absorption spectroscopy evidenced charge transfer between Pt and the supports. This approach allowed ascribing the changes in electrocatalytic activity for oxygen reduction solely to the variations in the electronic vacancy of the Pt 5d band resulting from the interactions between the metal nanoparticles and the supports containing different transition metal oxides. Oxygen reduction was studied in acid and in alkaline solutions, and linear correlations between the kinetic current densities and the Pt 5d band vacancy of pure Pt nanoparticles were found in both media. Possible first steps of the reduction of oxygen are discussed to explain the trends observed. The results, evidencing that enhanced ORR activity on Pt particles is promoted by a lower 5d band vacancy in acid solutions and by a higher one in alkaline medium, provide new insights on the fundamental aspects of oxygen reduction, and open up new possibilities to develop catalysts with enhanced activity for fuel cell cathodes by tuning their electronic properties.

Received 5th November 2018
Accepted 18th December 2018

DOI: 10.1039/c8ta10642h

rsc.li/materials-a

Introduction

The oxygen reduction reaction (ORR) is one of the most relevant electrochemical processes in energy conversion. Despite the progress made regarding the performance of low temperature fuel cells, the ORR, which takes place at the cell cathode, has remained a cause of large voltage losses that result from its very sluggish kinetics even on Pt, which is the most active metal for this reaction in acid solutions. Research aiming to develop high-performance ORR catalysts has been quite intense over the last few decades, and many papers were devoted to the study of Pt-based systems, such as PtCo,[1–5] PtFe,[3,5–7] PtNi,[1,5,8,9] PtCu,[8,10,11] PtCr,[5,12–14] and PtV,[5,14–16] that generally exhibit enhanced ORR activity as compared with Pt/C. Over the years, the ORR activity enhancement promoted by the addition of a second metal has been attributed to more favorable Pt–Pt nearest-neighbor distances,[17] to structural and electronic properties,[18,19] and to a reduction of coverage of the Pt surface by OH species.[19–22] The particle size, shape, structure and composition of Pt-based bimetallic catalysts also influence considerably the ORR activity.[23] The analysis of the individual effects of those different properties is, however, a long-standing difficulty because, more often than not, they are interdependent for nanoparticles. For instance, varying the composition of PtFe nanoparticles of similar sizes not only alters the lattice parameter and, thus, the Pt–Pt distance but also promotes changes in the electronic vacancy of the Pt 5d band,[24] while variations in size and alloying produced by heat treatments also affect the electronic properties of Pt.[6,16] Improvements in ORR activity were also reported for Pt nanoparticles on different supports, such as oxides[25–28] and carbon-oxide hybrids.[20,29–34] Strong metal–support interactions (SMSI)[35] inducing electronic effects were invoked to explain the effects of supports on ORR activity,[29,33] even though

[a]São Paulo State University (UNESP), Institute of Chemistry, Rua Prof. Francisco Degni, 55 – 14800-060 Araraquara, São Paulo, Brazil. E-mail: mercedes.villullas@unesp.br
[b]Helmholtz-Zentrum Berlin für Materialien und Energie, BESSY-II, Albert-Einstein-Straße 15, 12489, Berlin, Germany
[c]Brazilian Nanotechnology National Laboratory (LNNano), Brazilian Center for Research in Energy and Materials (CNPEM), Campinas, São Paulo, Brazil

† Electronic supplementary information (ESI) available. See DOI: 10.1039/c8ta10642h

‡ Present address: University of Campinas (Unicamp), Institute of Chemistry. Inomat – Bloco J, Cidade Universitária, 13083-970 Campinas, São Paulo, Brazil, CP 3154.

compressive strain[36] and alloy formation[37] were also proposed. In most cases, however, the enhanced ORR activity promoted by different supports is attributed to electronic effects although, more often than not, on a merely speculative basis because experimental data on electronic properties are seldom reported. Recent reviews on the ORR on Pt-based catalysts[38–43] and on support effects are available.[44–46]

Oxygen reduction is a complex process and no agreement has been reached regarding the details of the reaction mechanism and the rate-determining step. Nonetheless, a consensus seems to have been reached regarding the two main pathways,[47] the direct 4-electron reduction to water and the peroxide pathway:

$$O_2 + 4H^+ + 4e^- \rightarrow 2H_2O \text{ (direct pathway)} \quad (1)$$

$$O_2 + 2H^+ + 2e^- \rightarrow H_2O_2 \text{ (peroxide pathway)} \quad (2)$$

The H_2O_2 formed in reaction (2) can be further reduced to water or disproportionate:

$$H_2O_2 + 2H^+ + 2e^- \rightarrow 2H_2O \quad (3)$$

$$2H_2O_2 \rightarrow 2H_2O + O_2 \quad (4)$$

The equivalent reactions in alkaline solutions are:

$$O_2 + 2H_2O + 4e^- \rightarrow 4OH^- \text{ (direct pathway)} \quad (5)$$

$$O_2 + H_2O + 2e^- \rightarrow HO_2^- + OH^- \text{ (peroxide pathway)} \quad (6)$$

$$HO_2^- + H_2O + 2e^- \rightarrow 3OH^- \quad (7)$$

$$2HO_2^- \rightarrow 2OH^- + O_2 \quad (8)$$

The experimental data gathered over several decades suggest that the ORR on Pt and Pt-based alloys takes place through parallel direct and peroxide pathways, with the reaction going mainly through the 4-electron route, in both media. Several series-parallel mechanisms were proposed.[48–52]

The fundamental challenge of developing highly active ORR catalysts is still strongly dependent on advances regarding property–activity correlations. Clearly, changes in the electronic properties of an active metal might modify the strength with which different species adsorb on its surface and, in turn, alter the catalytic activity of that metal for electrochemical reactions involving adsorption of reactants and/or intermediates, as in the ORR. Unfortunately, experimental measurements for direct assessment of electronic properties are still rare. Herein, we present a systematic assessment of the effects of the electronic properties of pure Pt nanoparticles on the ORR activity by tuning the 5d band electronic vacancy by incorporating transition metal oxides into the support. It is demonstrated, for the first time, that the ORR kinetically controlled current densities on Pt nanoparticles of similar size and shape, *i.e.*, in the absence of composition and particle size and/or shape changes, vary linearly with the Pt 5d band electronic occupancy.

Experimental

Preparation of catalysts

Pt nanoparticles were synthesized in dioctyl ether by a modified polyol process[4,53] by reducing the metal precursor with 1,2-hexadecanediol in the presence of commercial nanopowders of transition metal oxides. Concisely, 80.7 mg of platinum(II) acetylacetonate (Sigma-Aldrich, 97%) and 16.1 mg of 1,2-hexadecanediol (Sigma-Aldrich, technical grade, 90%) were dissolved in 10 mL of dioctyl ether (Sigma-Aldrich, 99%) and kept constantly stirred under an Ar atmosphere. The solution was then heated up to 110 °C and then 32.0 mg of nanopowder of the transition metal oxide dispersed in 5 mL of dioctyl ether was added. After 5 minutes, 273 μL of oleic acid (Sigma-Aldrich, technical grade, 90%) and 394 μL of oleylamine (Sigma-Aldrich, technical grade, 70%) were added. After the addition of the capping agents, the temperature was kept at 110 °C for 15 minutes and then it was raised until reflux (about 298 °C). After 30 min under reflux to complete the reduction of Pt, the heating was stopped and the system was left to cool to room temperature. The solid (Pt/MO_x) was flocculated adding ethanol and separated from the reaction medium by centrifugation (9000 rpm). The Pt/MO_x material was then redispersed in a hexane + ethanol mixture and centrifuged again. These last steps (redispersion and centrifugation) were repeated until obtaining a colorless supernatant. In sequence, a dispersion of the Pt/MO_x powder in hexane was mixed with a dispersion of carbon powder (Vulcan XC-72, Cabot Corp.) in isopropanol. This mixture was kept under stirring overnight. Then, the obtained $Pt/MO_x/C$ catalyst was separated by filtration and washed thoroughly with ethanol, acetone and water. Subsequently, the $Pt/MO_x/C$ material was dispersed in ethanol another time, filtered and washed again with ethanol, acetone and water. This procedure was repeated twice. Finally, the catalyst was dried in an oven at 80 °C for 2 h.

All $Pt/MO_x/C$ catalysts were prepared with 20 wt% Pt loading and with a transition metal oxide to carbon proportion of 20 : 80 wt%. The particle sizes of commercial nanopowders of transition metal oxides (Sigma-Aldrich) were <50 nm for CeO_2 and TiO_2 and <100 nm for ZrO_2, SnO_2 and WO_3.

Catalyst characterization

XRD measurements were done with Rigaku Ultima IV equipment, model Ru200B using Cu Kα radiation (1.5406 Å) and recorded at 0.5 degrees per min for 2θ values between 20° and 100°.

The catalyst morphology was investigated by the acquisition of high-resolution images using an aberration corrected transmission electron microscope FEI Titan Themis Cubed 60-300 operating at 300 kV. The images were acquired in scanning mode (HR-STEM). The samples were prepared by directly applying the catalyst powder onto standard Cu TEM grids.

XPS spectra were collected with a K-ALPHA surface analysis spectrometer (Thermo Scientific, Inc.) using monochromatic Al Kα (1486.7 eV) as the photon source, in constant energy analyzer mode with an energy pass of 30 eV and energy steps of 0.1 eV. A

sample of Au/C was also analyzed to estimate the instrumental broadening, which was later used for the deconvolution of spectra of all other samples. In all cases, a Shirley background was subtracted and spectra were corrected using the C 1s core-line (284.5 eV) as the reference. For deconvolution, a Lorentzian function was used for all non-metallic components and a Doniach-Sunjic function (*i.e.*, asymmetric)[54,55] was used for all metallic components. For the fitting procedure the asymmetry parameter, αDS, was left to vary between 0.18 and 0.22, based on reported values for Pt.[56,57] The full width at half maximum (fwhm) for each component was determined for the Pt/C material and the values obtained were used for all the Pt/MO_x/C catalysts.

In situ X-ray absorption spectroscopy (XAS) experiments were carried out around the Pt L3 edge (11 564.25 eV, $2p_{3/2} \rightarrow 5d$ transitions) at the XAFS1 beamline of the Brazilian Synchrotron Light Laboratory (LNLS). Measurements were carried out using the catalyst as the working electrode in a spectroelectrochemical cell similar to that described in the literature.[58] For that, a mixture of 30 mg of catalyst powder and 400 μL of Nafion® solution (Aldrich, 5 wt% in a mixture of alcohols and water) was pressed on a carbon cloth. All working electrodes were prepared with a Pt loading of 6 mg cm^{-2}. A Pt mesh and a reversible hydrogen electrode were employed as auxiliary and reference electrodes, respectively. Spectra were collected while the catalysts were kept polarized at a constant potential (0.55, 0.80 and 0.90 V *vs.* RHE) in acid (0.5 M H_2SO_4) and in alkaline (0.1 M KOH) solutions. Normalization of spectra was done with the program Athena of the Demeter software package,[59] which was also used to determine the Pt L3 edge energy of all raw spectra from the zero crossing of the second derivative.

Electrochemical measurements

A conventional three-compartment electrochemical cell was used for all the experiments. Cyclic voltammetry (CV) experiments were carried out in the potential range of 0.05 V to 1.0 V in argon-saturated solution (0.5 M H_2SO_4 and 0.1 M KOH) at a scan rate of 50 mV s^{-1}. The electrocatalytic activity for the ORR was studied in O_2-saturated solution using the rotating ring disk electrode (RRDE) technique. The RRDE electrode consisted of a glassy carbon disk (0.247 cm^2) and a platinum ring (0.187 cm^2) and had a collection efficiency of 0.37 (Pine Research Instrumentation).

The catalysts were used in the form of an ultrathin layer, which was obtained by depositing 13 μL of catalyst ink on a glassy carbon disk. The catalyst ink was prepared with 2.9 mg of catalyst powder, 1.0 mL of isopropanol and 15 μL of Nafion® solution. The metal load on the working electrode was 28 μg cm^{-2}. A platinized platinum wire was used as the counter electrode and potentials were measured against a reversible hydrogen reference electrode. The ORR polarization curves were recorded in the potential range of 0.1 V to 1.0 V at different rotation rates and a sweep rate of 5 mV s^{-1}, while the hydrogen peroxide formed during the reduction of oxygen was monitored by its oxidation current on the Pt ring, which was kept polarized at 1.2 V. All electrochemical measurements were carried out at room temperature.

Results and discussion

Catalyst properties

X-ray diffraction analysis showed for the Pt/C catalyst the signals typical of the face centered cubic (fcc) structure of Pt (JCPDS 4-802) at 2θ about 40, 46, 67 and 81° as well as the one characteristic of the carbon support at 2θ around 25°. For Pt/MO_x/C catalysts, several of those signals overlap with those of the transition metal oxide. However, comparison of the diffraction patterns of Pt/MO_x/C catalysts and Pt/C showed that the 2θ position could be compared with minimal interference of the oxide signals for at least one Pt diffraction signal, as illustrated in Fig. 1 for Pt/CeO_2/C. In this case, it is seen that no signals of CeO_2 appear in the region of the diffraction peak of the [111] planes of Pt (2θ about 40°). Comparisons of diffraction patterns like that of Fig. 1 are shown for Pt/TiO_2/C, Pt/SnO_2/C, Pt/ZrO_2/C and Pt/WO_3/C in Fig. S1.† From the positions of the Pt diffraction peaks less affected by the signals (at 2θ about 40, 46, or 67° depending on the catalyst) it is apparent that the Pt signals appear at the same 2θ values, allowing to rule out the formation of the PtM alloy.[37] Additionally, these comparisons suggest that Pt nanoparticles have similar crystallite sizes.

Thus, the average crystallite diameter (D) was estimated for Pt/C using the Scherrer eqn:

$$D = \frac{0.9\lambda}{\omega \cos \theta} \quad (9)$$

where λ is the X-ray wavelength (1.54056 Å) and θ is the angle of the Bragg reflection. The crystallite mean size was found to be 2.5 nm.

The images obtained by HR-STEM showed that for all catalysts, most of the Pt nanoparticles are deposited on the transition metal oxide forming small aggregates, as shown for Pt/ZrO_2/C and Pt/CeO_2/C in Fig. 2. As can be seen, Pt nanoparticles seem to have similar sizes. In general, some Pt particles are also seen on the carbon support for all materials. Images of other catalysts are shown in Fig. S2.†

The average particle diameter was estimated from a size distribution histogram for Pt/C and it was found to be 3.1 ± 0.4 nm (Fig. S3†). Close examination and comparison of several

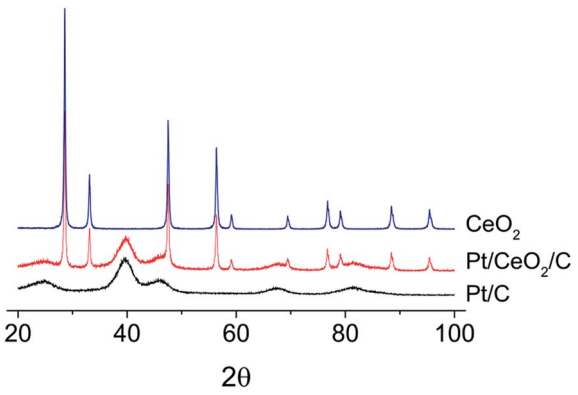

Fig. 1 Comparison of diffraction patterns of Pt/CeO_2/C with those of Pt/C and CeO_2.

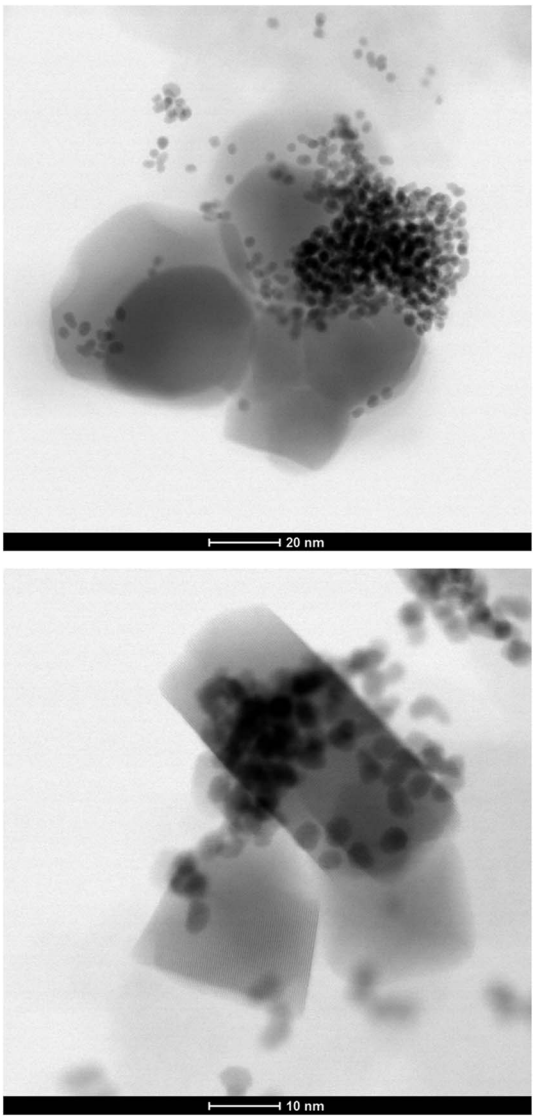

Fig. 2 HR-STEM images obtained in the bright field for $Pt/ZrO_2/C$ (top) and $Pt/CeO_2/C$ (bottom).

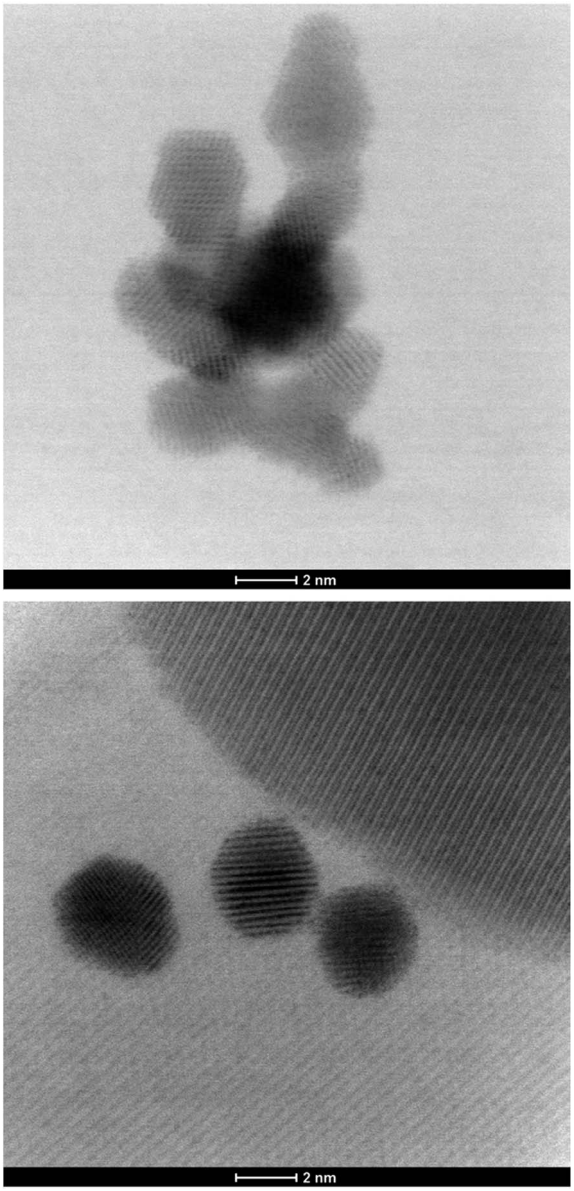

Fig. 3 HR-STEM images of Pt nanoparticles. Pt/C (top) and $Pt/ZrO_2/C$ (bottom).

images taken for each material revealed that Pt nanoparticles have a similar shape and size (about 3 nm) for all the $Pt/MO_x/C$ catalysts and Pt/C, as exemplified by Fig. 3, which shows Pt particles on Pt/C and on the carbon of the $Pt/ZrO_2/C$ catalyst.

The XPS Pt 4f spectra of all materials were fitted using one component corresponding to Pt^0 and two components corresponding to oxidized states (Pt^{n+}). The fitted curves are depicted in Fig. 4. The shifts of the Pt^{n+} components with respect to Pt^0 are 1 eV and 1.7 eV. These components have been attributed in the literature to Pt^{2+} and Pt^{4+} species, respectively.[60]

Binding energies, asymmetry parameters (αDS) and the calculated atomic percentages of Pt^0 and Pt^{n+} species are given in Table 1. It is interesting to note that the binding energy of all Pt species does not change for the different transition metal oxide supports. These results are in good agreement with data reported for Pt particles on hybrid $C–MO_x$ supports,[61] but differ from those reported for $Pt/TiO_2/C$ and $Pt/WO_3/C$[29] and those published for Pt/TiO_2, and $Pt/M–TiO_2$ (M = V, Cr, and Nb)[62] that showed a lowering of binding energy as compared with Pt/C. On the other hand, the amount of Pt^{n+} species is slightly smaller for the $Pt/MO_x/C$ catalysts than for Pt/C.

Cyclic voltammetry of $Pt/MO_x/C$ catalysts

The CV curves recorded at 50 mV s^{-1} in 0.5 M H_2SO_4 solution are shown in Fig. 5a, which evidences that curves for $Pt/MO_x/C$ and Pt/C are alike. The electrochemically active area (EAA) of Pt was calculated from the charge of oxidation of adsorbed hydrogen (0.210 mC cm^{-2}), which was obtained by integrating the anodic current up to ~0.35 V, after accounting for the double-layer contribution. The obtained values (*ca.* 2 cm^2, which corresponds to approximately 8.1 cm^2 of Pt per cm^2 of electrode geometric area) indicate that Pt EAAs for $Pt/MO_x/C$

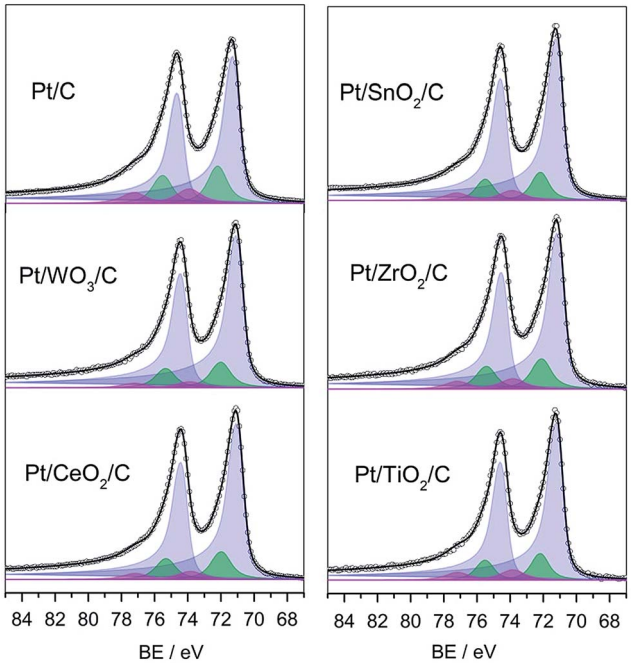

Fig. 4 Fitting of the Pt 4f photoemission spectra of Pt/C and Pt/MO_x/C catalysts. Components are Pt^0 (violet) and Pt^{n+} (green and pink).

Table 1 Results obtained from fitting the Pt 4f photoemission spectra. The values in parentheses correspond to the value obtained for the asymmetry parameter (αDS)

Catalyst	Pt $4f_{7/2}$ BE/eV and (αDS)	Specie	At%
Pt/C	71.3 (0.2)	Pt^0	75.9
	72.2	Pt^{n+}	24.1
	73.9		
Pt/SnO_2/C	71.2 (0.2)	Pt^0	83.0
	72.2	Pt^{n+}	17.0
	73.9		
Pt/TiO_2/C	71.2 (0.19)	Pt^0	82.7
	72.2	Pt^{n+}	17.3
	73.8		
Pt/ZrO_2/C	71.1 (0.21)	Pt^0	80.8
	72.1	Pt^{n+}	19.2
	73.8		
Pt/CeO_2/C	71.1 (0.21)	Pt^0	82.4
	72.1	Pt^{n+}	17.6
	73.9		
Pt/WO_3/C	71.1 (0.21)	Pt^0	84.4
	72.1	Pt^{n+}	15.6
	74.0		

catalysts and for Pt/C are similar (within less than 10%), as shown in Fig. 5b. These results are in good agreement with Pt particles having similar sizes for all materials, as evidenced by analysis of HR-TEM images.

Oxygen reduction in acid medium

A comparison of ORR polarization curves for Pt/MO_x/C and Pt/C catalysts is shown in Fig. 6. RRO polarization curves and the

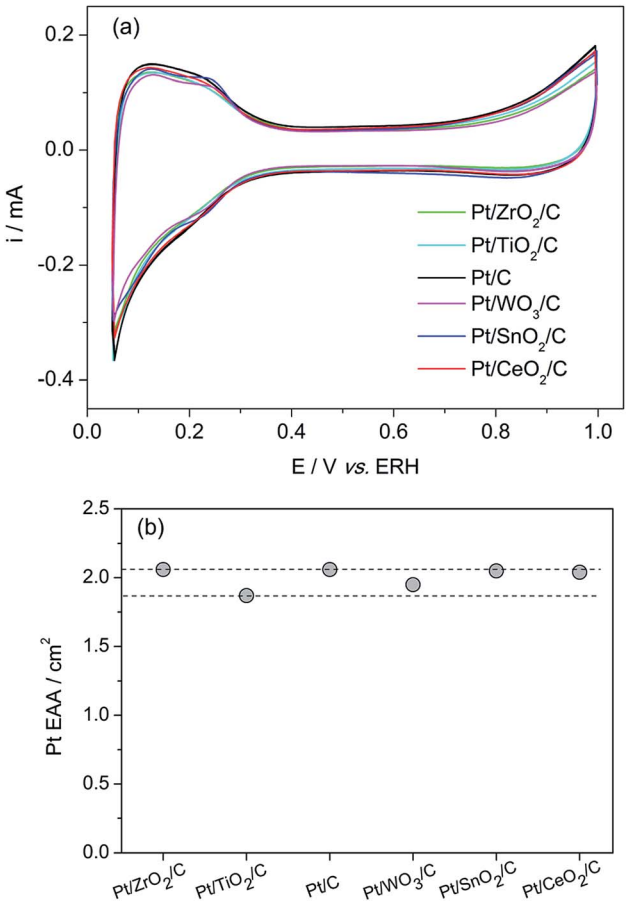

Fig. 5 (a) CV curves recorded for Pt/MO_x/C and Pt/C catalysts in 0.5 M H_2SO_4 at 50 mV s^{-1}. (b) Pt EAA values calculated from the charge of hydrogen desorption for all catalysts.

currents of hydrogen peroxide oxidation were recorded at different rotation rates for each catalyst (Fig. S4†). A shift of the ORR polarization curve towards higher potentials is clearly seen in Fig. 6 for Pt/SnO_2/C and Pt/CeO_2/C. The behavior of a RDE with its surface modified by nanoparticles was modelled by Masa *et al.*[63] that showed that a positive half-wave potential ($E_{1/2}$) shift could result not only from a catalytic improvement (better intrinsic activity) but also from a higher electroactive surface area. For the Pt/MO_x/C catalysts studied in this work, the Pt EAA is nearly the same (Fig. 5b) and, therefore, the $E_{1/2}$ shifts of *ca.* 20 and 40 mV observed, respectively, for Pt/SnO_2/C and Pt/CeO_2/C as compared with Pt/C evidence enhanced electrocatalytic activity.

The number of electrons transferred in the potential region of mixed kinetic-diffusion control can be estimated using the Koutecky–Levich equation:

$$\frac{1}{i} = \frac{1}{i_k} + \frac{1}{i_L} \quad (10)$$

where i is the measured current, i_k the kinetic current and i_L is the diffusion-controlled or limiting current given by the Levich equation

$$i_L = 0.62nFAD^{2/3}\nu^{-1/6}C_o\omega^{1/2} \quad (11)$$

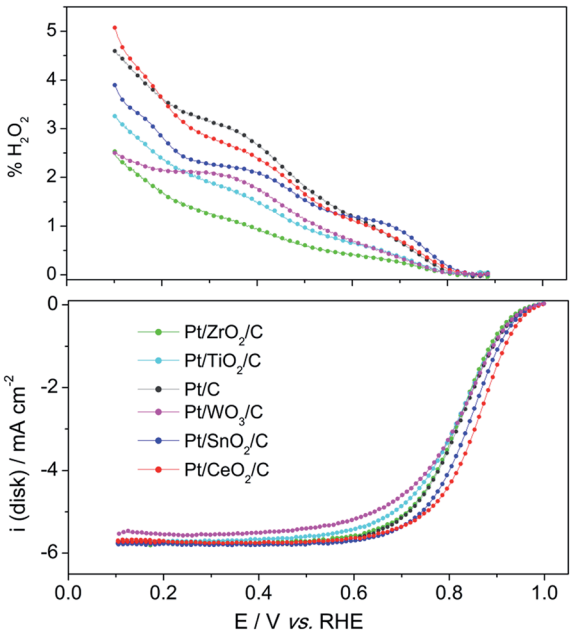

Fig. 6 ORR polarization curves measured at the disk electrode in O_2-saturated 0.5 M H_2SO_4 solution and H_2O_2 yield. Scan rate: 5 mV s^{-1}. Rotation rate: 2500 rpm. Currents normalized by the geometric area of the disk electrode (0.247 cm^2).

where n is the number of electrons transferred in the reaction, A is the disk electrode area, D is the diffusion coefficient of the reacting species, n is the kinematic viscosity of the electrolyte, C_o is the bulk concentration of electroactive species, ω is the rotation rate in rad s^{-1}, and F is the Faraday constant. In the region of mixed kinetic-diffusion control, the so called Koutecky–Levich plots (i^{-1} against $\omega^{-1/2}$) showed parallel lines with slopes close to the expected value for 4 electrons, in good agreement with the literature for Pt materials.[47] Some Koutecky–Levich plots are shown in Fig. S5.†

The hydrogen peroxide yield (% H_2O_2) was calculated with eqn (12).

$$H_2O_2(\%) = \left(\frac{2i_r/N}{i_d + i_r/N}\right) \times 100\% \quad (12)$$

where i_d is the ORR current measured at the disk, i_r is the current of oxidation of H_2O_2 measured at the ring electrode, and N is the RRDE collection efficiency (0.37). Another advantage of the RRDE as compared with the RDE is that it allows obtaining the number of electrons (n) as a function of potential directly from the measured currents at the disk and ring electrodes using eqn (13):[64,65]

$$n = \left(\frac{4i_d}{i_d + i_r/N}\right) \quad (13)$$

Thus, the peroxide yield and the number of electrons are related as:[64,65]

$$H_2O_2(\%) = 100 \times \left(\frac{4-n}{2}\right) \quad (14)$$

As seen in Fig. 6, for all catalysts, the H_2O_2 yield is smaller than 1% between 0.9 and 0.7 V and it stays below 5% even in the potential region where the ORR current is diffusion-controlled. The number of electrons calculated from the RRDE currents is shown as a function of potential in Fig. 7, which clearly evidences that the RRO proceeds predominantly through the 4-electron pathway.

The kinetic currents were calculated from the measured and diffusion limited values using eqn (10). In order to compare intrinsic activities, current densities were obtained by normalizing by the Pt EAA. Fig. 8a and b show the ORR kinetic current densities at 0.90 V and 0.8 V, respectively. At both potentials, higher values of kinetic current density are obtained for the ORR on Pt/CeO_2/C and Pt/SnO_2/C catalysts while the values for Pt/WO_3/C and Pt/C are similar.

Fig. 9 shows the mass-transport corrected Tafel plots for Pt/CeO_2/C and Pt/ZrO_2/C, which exhibit slopes of −60 mV dec^{-1} and −120 mV dec^{-1} in the regions of low and high currents, respectively. This slope variation is well known for polycrystalline Pt,[47] Pt low index surfaces,[66,67] and carbon-supported Pt and Pt alloys.[6,68] Although a Tafel slope change would be expected if the rate-determining step changes, there is a consensus that this is not the case for the ORR on Pt and the change is attributed to the potential dependence of the coverage of adsorbed oxygen-containing species.[47,66] Similar Tafel plots were obtained for other Pt/MO_x/C materials (Fig. S6†). Thus, considering that all Tafel plots are alike, the ORR rate-determining step is likely to be the same on all catalysts.

Electronic properties

Normalized *in situ* XAS spectra taken around the Pt L3 edge in 0.5 M H_2SO_4 solution are shown in Fig. 10a. In general, spectra show that the intensity of the absorption peak varies for the different Pt/MO_x/C catalysts. In order to compare the electronic properties on a more quantitative basis, the XANES (X-ray Absorption Near Edge Structure) region of the spectrum was fitted combining a Lorentzian curve with an arc tangent curve, as proposed by Shukla *et al.*,[7] to account for transitions to bound states and to the continuum, respectively. To make comparisons of the Pt 5d band electronic vacancy, the Lorentzian curve fitted is then integrated (a larger electronic vacancy leads to higher absorption and, consequently, larger

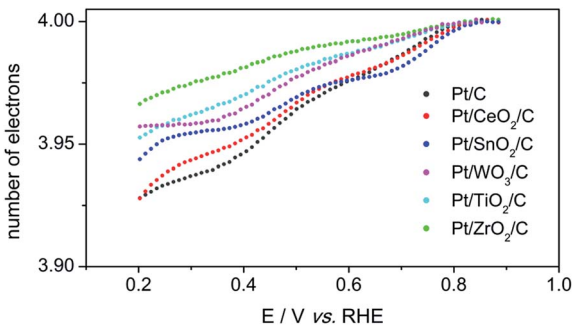

Fig. 7 Number of electrons calculated from RRDE currents measured in 0.5 M H_2SO_4 solution as a function of potential.

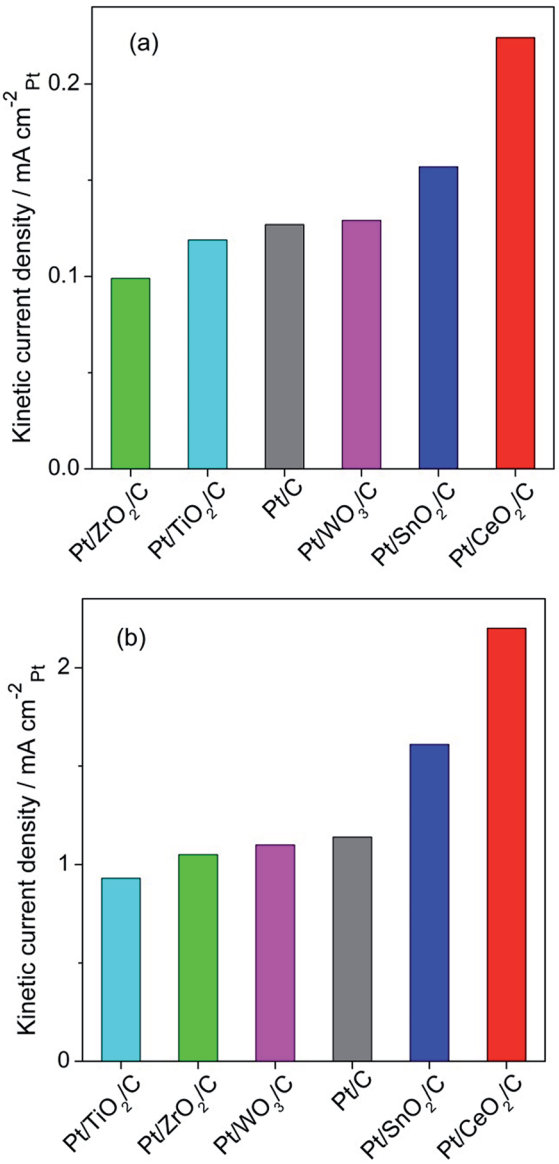

Fig. 8 (a) Kinetic current density of the ORR at the different Pt/MO_x/C and Pt/C catalysts at 0.90 V. (b) Results at 0.80 V.

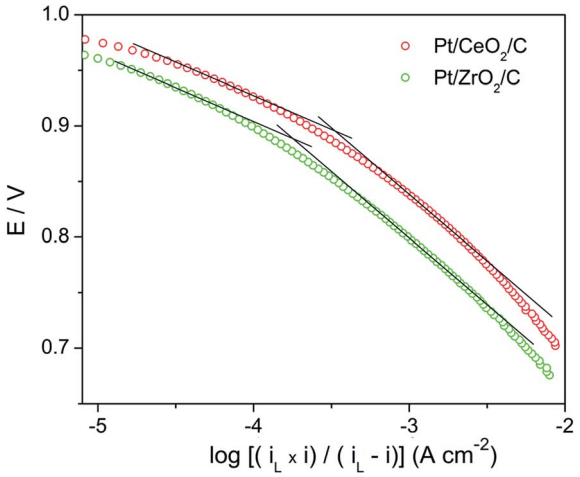

Fig. 9 Tafel plots for Pt/CeO_2/C and Pt/ZrO_2/C catalysts. The lines correspond to −60 mV dec^{-1} and −120 mV dec^{-1}. Kinetic current densities obtained by normalizing by the Pt EAA.

values of the integral of the Lorentzian curve[18,69]). The results obtained from treating the XANES region of spectra collected at three different applied potentials are depicted in Fig. 10b.

For all catalysts, the growth of the integral of the fitted Lorentzian curve as the applied potential is raised indicates an increase in the Pt 5d band vacancy, in agreement with previous literature reports for carbon supported Pt[18,70,71] and Pt alloys.[16,72] This electronic vacancy increase with applied potential has been interpreted as due to the effect of oxygenated species adsorbed on the Pt surface.[18] We must point out that XAS data for the Pt/WO_3/C catalyst were not included in Fig. 10 because the proximity of the W L2 absorption signal prevents treatment. As observed for other catalysts, the rise of applied potential promotes an increase in the absorption intensity around the Pt L3 that evidences an increase in the Pt 5d band vacancy. In contrast, no significant changes were seen for the W L2 absorption (Fig. S7†). Altogether, Fig. 9 reveals that the electronic vacancy of the Pt 5d band is lower for Pt/CeO_2/C and Pt/SnO_2/C and higher for Pt/TiO_2/C and Pt/ZrO_2/C, as compared to Pt/C.[18,69] Thus, there is charge transfer to the Pt 5d orbital for SnO_2/C and CeO_2/C supports, and from the Pt 5d orbital to TiO_2/C and ZrO_2/C.

It is noteworthy that direct probe of the Pt 5d band electronic vacancy by XAS evidences that changes induced by the interaction of the Pt particles with the MO_x/C supports promote a shift in the Fermi level of Pt that results in new electronic states (vacant or filled). Comparison with XPS data discussed above, however, clearly demonstrates that not always these electronic changes are enough to promote variations of binding energies, in agreement with previously published data.[61]

Electronic effects in oxygen reduction

Data depicted in Fig. 8 demonstrate that the transition metal oxide incorporated into the support influences the ORR activity of Pt nanoparticles, while results shown in Fig. 10 indicate that there is also an effect on the electronic occupancy of the Pt 5d band. Several papers have attributed the changes in ORR activity on Pt-based catalysts, such as PtFe, PtNi and PtCo, to the variation of electronic properties with the second metal content.[19,24] Although ORR results showed a correlation with the electronic properties, the variation of composition of the catalysts also involved changes in the lattice parameters that, in turn, could alter the adsorption of the O_2 molecule. For instance, for a set of Pt alloy catalysts Mukerjee *et al.*[18] observed a volcano-type dependence of the logarithm of the ORR current density at 0.90 V with the Pt–Pt distance as well as with the Pt d-band vacancy of Pt, concluding that the catalysts at the top of the curve have the best combination of electronic properties and geometric parameters. For Pt-based catalysts, Toda *et al.*[19] observed a volcano-type variation of the ORR kinetic current density with the atomic percentage of Fe, Co and Ni, which was interpreted in terms of changes of the d-band vacancy with

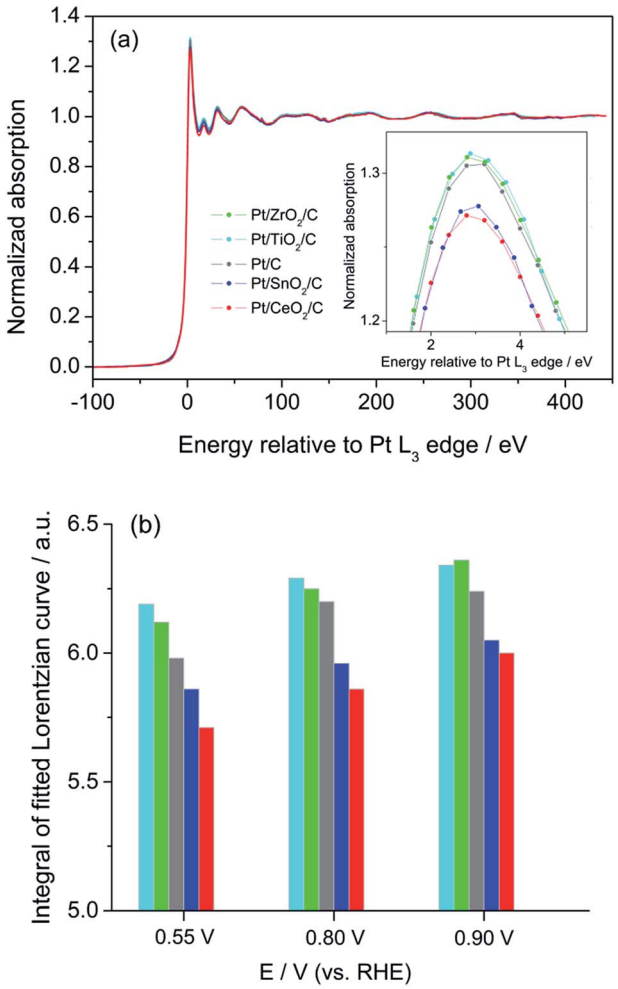

Fig. 10 (a) Normalized *in situ* XAS spectra of Pt/MO_x/C and Pt/C catalysts obtained in 0.5 M H_2SO_4 at 0.90 V. Inset: region of maximum intensity enlarged. (b) Values of the integral of the Lorentzian curve adjusted to the XAS spectra measured at different applied potentials. Pt/ZrO_2/C (green), Pt/TiO_2/C (light blue), Pt/C (gray), Pt/SnO_2/C (blue), and Pt/CeO_2/C (red).

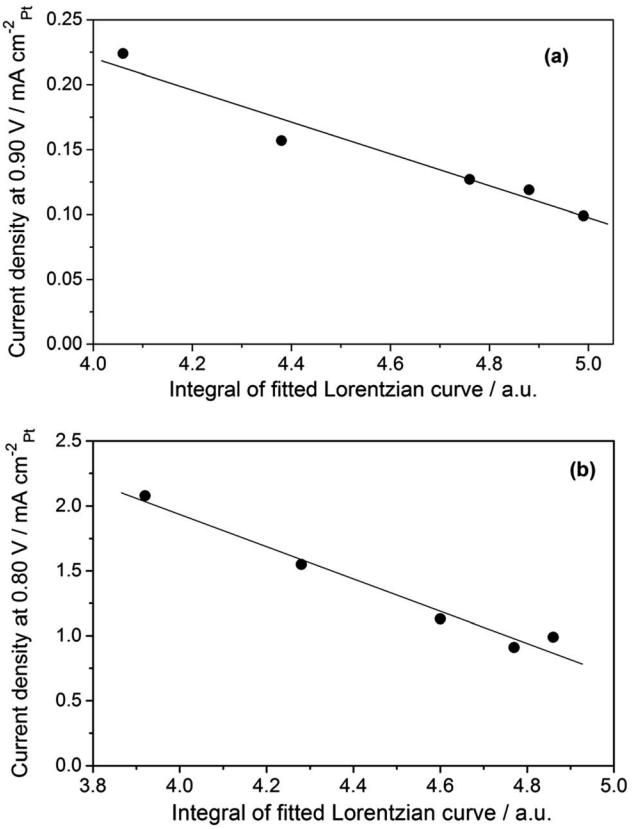

Fig. 11 Kinetic current densities of oxygen reduction at (a) 0.90 V and (b) 0.80 V against the values of the integral of the Lorentzian curve adjusted to the *in situ* XAS spectra measured at those potentials in 0.5 M H_2SO_4. Larger values of integral of the Lorentzian curve correspond to a higher Pt 5d band electronic vacancy. Pearson's coefficients of linear fit: 0.976 (0.90 V) and 0.986 (0.80 V).

composition. Keeping in mind that surface as well as electronic properties are relevant in electrocatalysis,[73] the variation of properties other than the electronic vacancy of the Pt 5d band is likely to be the cause of opposite explanations for ORR enhanced activity, which was attributed, at least partially, to a higher[19,24] and to a lower[15,72] Pt d-band vacancy.

Thus, it is pertinent to emphasize again that Pt/MO_x/C catalysts studied in this work have the same loading of pure Pt nanoparticles with similar sizes and shapes, minimizing variations of surface properties, and that the Pt EAA is nearly the same. The kinetic current densities of oxygen reduction at 0.80 V and 0.90 V show a good linear correlation with the values of the integral of the Lorentzian curve adjusted to the *in situ* XAS spectra measured at those potentials, as illustrated in Fig. 11. The change in kinetic current density is about twofold at both potentials, revealing that a decrease in the electronic vacancy of the Pt 5d band enhances the ORR activity.

The results reported for Pt/C and Pt–Co/C catalysts showed a linear correlation between the ORR activities at 0.9 V determined from measurements in a PEM fuel cell at 80 °C and the electronic properties assessed from the Pt L3 XANES region,[72] but the particle size and Pt–Pt distance (alloying) in the catalysts studied had a simultaneous variation. The correlation found for Pt/C and Pt–Co/C catalysts evidenced that lowering the Pt 5d band electronic vacancy resulted in higher ORR currents, which were attributed to a reduced OH adsorption on Pt sites.[72] Also, Ho *et al.*[28] observed a significantly enhanced ORR activity for Pt on the $Ti_{0.7}Mo_{0.3}O_2$ support at the time that from XAS measurements at the Pt L3 edge concluded that this support produced a decrease in the Pt 5d band vacancy. Thus, it must be highlighted here that results shown in Fig. 11 show, for the first time, how the ORR activity on pure Pt nanoparticles depends on the 5d band electronic vacancy.

There are different views regarding the rate-determining step of the ORR. Some authors propose that the reaction begins with the O_2 adsorption ($O_2 \rightarrow O_{2(ads)}$).[47] The rate-determining step could be the breaking of the O–O bond. In this case, a strong interaction with the surface would promote a weakening of the bond and favor its scission. Sawyer and Seo[74] proposed in 1977

that the first step in the reduction of oxygen would be the one-electron reduction to the superoxide anion

$$O_2 + e^- \rightarrow O_2^- \quad (15)$$

According to the authors' analysis of the experimental evidence available at that time, the formation of the superoxide anion would be reversible and independent of the electrode material. In other words, it would be an outer-sphere electron transfer to an O_2 molecule. A superoxide adsorbed state was also considered as well as the possibility of an equilibrium of adsorbed and in solution O_2^-, particularly in alkaline media.[75] Some authors have proposed that the reaction might be initiated by the formation of superoxide (eqn (15)) and it has been considered that the ORR rate-determining step in the low and high current density regions would be the first electron transfer with formation of superoxide.[66] Some evidence of the formation of superoxide was obtained more than 30 years ago, for example, by analyzing solutions with an electron spin resonance spectrometer, with the ORR taking place in a flow-type thin layer cell.[75] Spectroscopic evidence of adsorbed O_2^- was reported later by Shao *et al.*[76] Another possibility often considered is the concomitant electron and proton transfer

$$O_{2(ads)} + H^+ + e^- \rightarrow HO_2 \quad (16)$$

The ORR data presented above evidence that the reaction takes place mainly through the direct 4-electron reduction of O_2 to H_2O, with the peroxide pathway occurring to a small extent. In addition, Fig. 10 demonstrates that the ORR activity is higher for materials with a higher electronic occupancy of the Pt 5d band. Different O_2 adsorption energies were considered the cause of the different ORR activities of Pt low index surfaces,[66] attributing the higher activity to a strong interaction of O_2 with the surface and the resulting lowering of the activation energy for dissociative adsorption. From that viewpoint, a stronger interaction of O_2 with Pt favoring the O–O bond breaking seems improbable as the cause of the enhancement of ORR activity on $Pt/MO_x/C$ catalysts exhibiting a higher d-band electronic occupancy. A more likely scenario would be that a less vacant d-band resulting in an inhibition of OH adsorption would contribute to keep Pt sites available for O_2 adsorption. However, that being the case, to consider that the bond breaking is the rate-determining step it would be necessary to assume that the same changes in the d-band vacancy responsible for the variations of OH coverage would have only a minor effect on the strength of the interaction of O_2 with Pt. This hypothesis seems questionable.

Now, let us consider the formation of O_2^- as the rate-determining step. First, we can rule out an outer-sphere reaction, which is not influenced by the electronic properties of the catalyst. Adsorbed O_2^- was detected for the ORR on Pt in alkaline solution by surface-enhanced infrared reflection absorption spectroscopy (SEIRAS).[76] The formation of adsorbed O_2^- from an adsorbed species was inferred from the dependence on the potential of the band ascribed to the stretching mode of the O–O bond.[76] These authors observed no signal indicative of adsorbed O_2^- in acid solution and that was interpreted as likely due to a rapid protonation of O_2^- causing a considerably shorter lifetime. In the present case, the formation of O_2^- as cause of the influence of the d-band electronic vacancy on the ORR kinetic current density depicted in Fig. 11 seems, therefore, unlikely.

Thus, we should consider simultaneous electron and proton transfer. In the case of a less vacant Pt 5d band, a weaker interaction of adsorbed O_2 could favor a rate increase of the reaction. This hypothesis seems compatible with the drop in activity with the increase in the Pt 5d band vacancy depicted in Fig. 11.

In summary, our data for $Pt/MO_x/C$ catalysts having an identical loading of similar pure Pt nanoparticles evidence quite clearly that the ORR takes place with formation of small amounts of H_2O_2. Tafel plots are alike suggesting that the reaction goes mainly through the same pathways on Pt/C and $Pt/MO_x/C$ catalysts. Electronic changes are induced by the interactions of the metal particles and hybrid supports, differing only in the transition metal oxide used, and have a significant effect on the activity for the ORR on Pt nanoparticles.

Oxygen reduction in alkaline solution

Measurements similar to those described above were also carried out in 0.1 M KOH solution and RRDE data are shown for all catalysts in Fig. S8.† The number of electrons transferred calculated from Koutecky–Levich plots for the different catalysts was found to be in the range of 3.7 to 4. Some Koutecky–Levich plots are depicted in Fig. S9.† A comparison of ORR polarization curves and H_2O_2 yields is shown in Fig. S10.† Fig. 12 depicts the kinetically controlled current at 0.90 V calculated with eqn (10). Comparison of values with those of Fig. 8a evidences that the catalysts are significantly more active in alkaline solution than in acid medium. On the other hand, differently than in an acid environment, in alkaline solution all $Pt/MO_x/C$ catalysts are

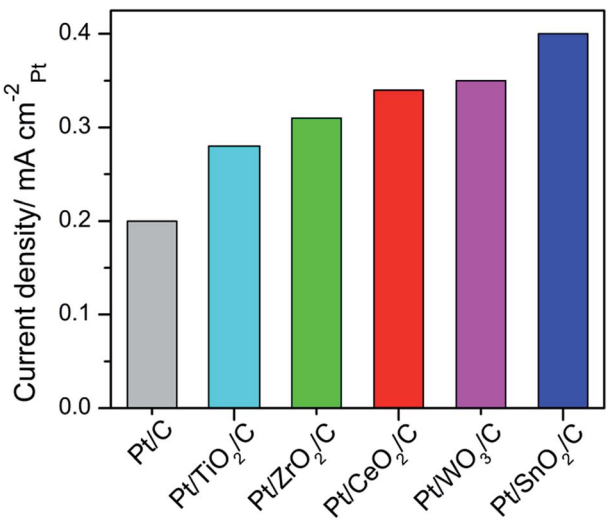

Fig. 12 Kinetic current densities of the ORR at 0.90 V in 0.1 M KOH. Kinetic current densities obtained by normalizing by the Pt EAA.

more active than Pt/C. The hydrogen peroxide yields in alkaline solution are somewhat higher than in acid medium. Nonetheless, for all catalysts the % H_2O_2 remains below 3% above 0.80 V, *i.e.*, until the beginning of the diffusion-controlled region. Consequently, the number of electrons (Fig. S11†) is very close to 4 in the region of interest for application (between 0.8 and 1.0 V) and higher than 3.75 in the limiting current region.

As observed in acid solution, the Tafel plots for Pt/C and Pt/MO_x/C catalysts are alike, as illustrated in Fig. 13, but the slopes are significantly smaller. The Tafel slope is −30 mV dec^{-1} in the region of very low currents and at higher currents it is −60 mV dec^{-1}. Slopes of −30 mV dec^{-1} changing to higher ones (ranging from −60 to −80 mV dec^{-1}) were reported for other systems in alkaline solution.[47] The results obtained suggest that the mechanism of the ORR in alkaline solution is the same for all catalysts although it seems to be different from the one in acid medium.

The *in situ* XAS measurements around the Pt L3 edge performed in 0.1 M KOH solution showed that for all Pt/MO_x/C catalysts the d-band vacancy is larger than that for Pt/C (Fig. S12†), contrasting with data taken in acid solution (Fig. 10b). The trend observed in alkaline solution is likely due to dissimilarities in the surface density of OH species adsorbed on the different transition metal oxides associated with diverse values of zeta potential. In principle, OH species adsorbed on the oxide surface could favor a drawing of electronic density from the oxide itself that, in turn, would promote a charge transfer from the Pt particles to the oxide. The relationship between the ORR kinetically controlled current density and the d-band vacancy is linear, as shown in Fig. 14, and reveals that the catalytic activity gets better as the Pt 5d band vacancy increases.

As discussed above, adsorbed O_2^- was detected for the ORR on Pt in alkaline solution, which appeared to be formed from adsorbed O_2.[76] For the ORR in alkaline media, Ramaswamy and Mukerjee[77] suggested that in alkaline media the adsorption of OH species not only blocks the sites for the adsorption of O_2 but also leads to an outer-sphere electron transfer mechanism. According to these authors, for Pt in alkaline media the outer-sphere charge transfer would take place only in the region of oxide formation and depending on the coverage of OH both inner- and outer-sphere mechanisms coexist for the ORR. Based on theoretical calculations for the ORR in alkaline solutions on Au and Ag surfaces, Ignaczak *et al.*[78] concluded that the more favorable path for the formation of adsorbed O_2^- from O_2 is through an outer-sphere charge transfer, and that O_2^- species adsorbed and in solution coexist at the equilibrium potential. However, extending the analysis to Pt(111) these researchers suggested that the adsorption of O_2 ($O_2 \rightarrow O_{2(ads)}$) and formation of adsorbed O_2^- ($O_{2(ads)} + e^- \rightarrow O_2^-{}_{(ads)}$) could take place simultaneously, and that the latter is probably more favorable than the outer-sphere reaction.[78]

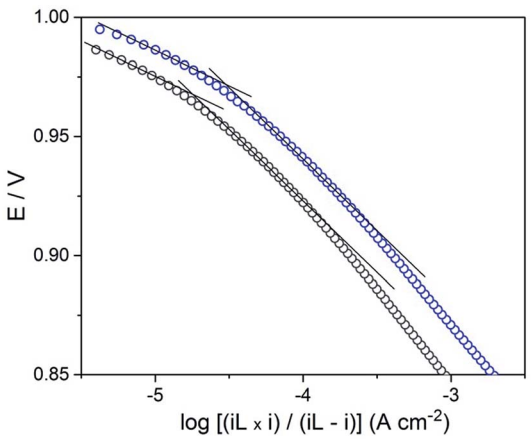

Fig. 13 Tafel plots for Pt/SnO_2/C (blue) and Pt/C (black). The lines correspond to −30 mV dec^{-1} and −60 mV dec^{-1}. Kinetic current densities obtained by normalizing by the Pt EAA.

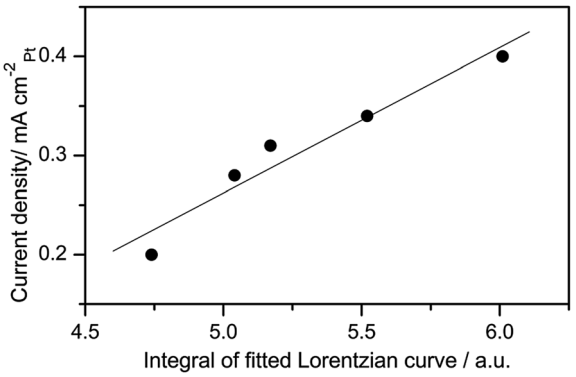

Fig. 14 Kinetic current densities of oxygen reduction at 0.90 V against the values of the integral of the Lorentzian curve adjusted to the *in situ* XAS spectra measured at those potentials in 0.1 M KOH. Pearson's coefficient of linear fit: 0.969.

Data depicted in Fig. 14 show an enhancement of ORR activity as the Pt 5d band vacancy increases. The donation of 2p electrons from adsorbed O_2 (or adsorbed O_2^-) to Pt would make the interaction stronger. As mentioned above, a stronger interaction would weaken the O–O bond easing its breaking and resulting in a higher reaction rate.[66]

Altogether, the results obtained in this work show that taking advantage of the changes induced by the interactions between the metal and transition metal oxides incorporated in supports it is possible to explore the effects of the electronic properties of pure Pt nanoparticles on the ORR activity. In the absence of composition and size and/or shape variations, it was demonstrated that the electrocatalysis of the ORR on Pt particles is favored by a lower 5d band vacancy in acid solutions and by a higher one in alkaline medium. The new understandings shed some light on the fundamental aspects of the electrocatalysis of the ORR on Pt particles and give new bases for developing catalysts with enhanced activity for fuel cell cathodes.

Conclusions

The properties of pure Pt nanoparticles with similar sizes and shapes were explored taking advantage of the changes induced

by the interactions between the metal and different transition metal oxides in the support, in the systematic study of Pt/MO_x/C catalysts having the same Pt loading (20 wt%). These materials were characterized by several techniques. XPS analysis showed that the binding energy of Pt species does not change for the different transition metal oxide supports. *In situ* XAS measurements demonstrated that the interactions of the Pt particles and MO_x/C supports induced changes in the Pt 5d band vacancy. In acid solutions, data show that the ORR takes place predominately through the direct 4-electron pathway for all Pt/MO_x/C catalysts. Tafel plots are alike for all materials, with slopes of -60 mV dec^{-1} and -120 mV dec^{-1} in the regions of low and high currents, respectively. The Pt 5d band electronic vacancy variations have a significant impact on the ORR activity. The kinetic currents evaluated at 0.90 and 0.80 V show a linear decrease as the Pt 5d band vacancy increases. In alkaline solution, ORR Tafel plots are also alike for all Pt/MO_x/C catalysts, but slopes at low and high currents are, respectively, -30 mV dec^{-1} and -60 mV dec^{-1}. The dependence of the ORR kinetic current is also linear, but in contrast with results for acid solution, the enhancement of activity follows an increase in the Pt 5d band vacancy. The effect of band vacancies on the ORR kinetic current density observed in acid solution is compatible with simultaneous electron and proton transfer upon oxygen adsorption being the rate-controlling step. In alkaline solution, the linear increase in catalytic activity with the Pt d-band vacancy can be ascribed to the stronger interaction of adsorbed O_2 (or O_2^-) with the surface promoting the breaking of the O–O bond. Overall, the results presented unveiled the relevance of the electronic properties in the electrocatalysis of the ORR on Pt nanoparticles.

The results reported contribute not just to increase our current understanding of the fundamental aspects of the ORR but also provide new bases for developing efficient catalysts for fuel cell cathodes by tuning their electronic properties. In this context, exploring the effects on the Pt d-band vacancy of supports containing other transition metal oxides as well as other compounds, such as carbides, seems highly desirable.

Conflicts of interest

There are no conflicts to declare.

Acknowledgements

The authors acknowledge the Brazilian agencies Fundação de Amparo à Pesquisa do Estado de São Paulo (FAPESP) (2014/12255-6) and Conselho Nacional de Desenvolvimento Científico e Tecnológico (CNPq), (407143/2013-0) for financial support. We also acknowledge the Brazilian Synchrotron Light Laboratory (LNLS) for the access that allowed X-ray absorption experiments, and the Brazilian Nanotechnology National Laboratory (LNNano) for XPS measurements and for the use of the FEI Titan Themis 60-300 microscope. The XAFS1 beamline staff is acknowledged for the assistance during the X-ray absorption measurements. FBO acknowledges the fellowship granted by Coordenação de Aperfeiçoamento de Pessoal de Nível Superior (CAPES).

References

1 U. A. Paulus, A. Wokaun, G. G. Scherer, T. J. Schmidt, V. Stamenkovic, V. Radmilovic, N. M. Markovic and P. N. Ross, *J. Phys. Chem. B*, 2002, **106**, 4181–4191.
2 J. R. C. Salgado, E. Antolini and E. R. Gonzalez, *J. Electrochem. Soc.*, 2004, **151**, A2143–A2149.
3 L. Xiong and A. Manthiram, *Electrochim. Acta*, 2005, **50**, 2323–2329.
4 E. I. Santiago, L. C. Varanda and H. M. Villullas, *J. Phys. Chem. C*, 2007, **111**, 3146–3151.
5 H. Yano, M. Kataoka, H. Yamashita, H. Uchida and M. Watanabe, *Langmuir*, 2007, **23**, 6438–6445.
6 A. R. Malheiro, J. Perez and H. M. Villullas, *J. Electrochem. Soc.*, 2009, **156**, B51–B58.
7 A. K. Shukla, R. K. Raman, N. A. Choudhury, K. R. Priolkar, P. R. Sarode, S. Emura and R. Kumashiro, *J. Electroanal. Chem.*, 2004, **563**, 181–190.
8 L. Xiong and A. Manthiram, *J. Electrochem. Soc.*, 2005, **152**, A697–A703.
9 E. Antolini, J. R. C. Salgado and E. R. Gonzalez, *J. Electroanal. Chem.*, 2005, **580**, 145–154.
10 E. A. Carbonio, F. Colmati, E. G. Ciapina, M. E. Pereira and E. R. Gonzalez, *J. Braz. Chem. Soc.*, 2010, **21**, 590–602.
11 M. Oezaslan, F. Hasche and P. Strasser, *J. Electrochem. Soc.*, 2012, **159**, B444–B454.
12 H. Yang, N. Alonso-Vante, J. M. Leger and C. Lamy, *J. Phys. Chem. B*, 2004, **108**, 1938–1947.
13 R. C. Koffi, C. Coutanceau, E. Garnier, J. M. Leger and C. Lamy, *Electrochim. Acta*, 2005, **50**, 4117–4127.
14 F. H. B. Lima, M. J. Giz and E. A. Ticianelli, *J. Braz. Chem. Soc.*, 2005, **16**, 328–336.
15 L. G. R. A. Santos, K. S. Freitas and E. A. Ticianelli, *Electrochim. Acta*, 2009, **54**, 5246–5251.
16 R. Gentil and H. M. Villullas, *J. Solid State Electrochem.*, 2016, **20**, 1119–1129.
17 V. Jalan and E. J. Taylor, *J. Electrochem. Soc.*, 1983, **130**, 2299–2301.
18 S. Mukerjee, S. Srinivasan, M. P. Soriaga and J. McBreen, *J. Electrochem. Soc.*, 1995, **142**, 1409–1422.
19 T. Toda, H. Igarashi, H. Uchida and M. Watanabe, *J. Electrochem. Soc.*, 1999, **146**, 3750–3756.
20 K. Sasaki, L. Zhang and R. R. Adzic, *Phys. Chem. Chem. Phys.*, 2008, **10**, 159–167.
21 V. Stamenkovic, T. J. Schmidt, P. N. Ross and N. M. Markovic, *J. Phys. Chem. B*, 2002, **106**, 11970–11979.
22 V. S. Murthi, R. C. Urian and S. Mukerjee, *J. Phys. Chem. B*, 2004, **108**, 11011–11023.
23 Y. J. Wang, N. N. Zhao, B. Z. Fang, H. Li, X. T. T. Bi and H. J. Wang, *Chem. Rev.*, 2015, **115**, 3433–3467.
24 A. R. Malheiro, J. Perez and H. M. Villullas, *J. Power Sources*, 2010, **195**, 7255–7258.
25 P. J. Kulesza, B. Grzybowska, M. A. Malik and M. T. Galkowski, *J. Electrochem. Soc.*, 1997, **144**, 1911–1917.

26 G. C. Abha Bharti, *J. Power Sources*, 2017, **363**, 413–421.
27 K. Kakinuma, Y. Chino, Y. Senoo, M. Uchida, T. Kamino, H. Uchida, S. Deki and M. Watanabe, *Electrochim. Acta*, 2013, **110**, 316–324.
28 V. T. T. Ho, C. J. Pan, J. Rick, W. N. Su and B. J. Hwang, *J. Am. Chem. Soc.*, 2011, **133**, 11716–11724.
29 A. Lewera, L. Timperman, A. Roguska and N. Alonso-Vante, *J. Phys. Chem. C*, 2011, **115**, 20153–20159.
30 K. Fugane, T. Mori, D. R. Ou, P. Yan, F. Ye, H. Yoshikawa and J. Drennan, *Langmuir*, 2012, **28**, 16692–16700.
31 T. Masuda, H. Fukumitsu, K. Fugane, H. Togasaki, D. Matsumura, K. Tamura, Y. Nishihata, H. Yoshikawa, K. Kobayashi, T. Mori and K. Uosaki, *J. Phys. Chem. C*, 2012, **116**, 10098–10102.
32 D. Takimoto, C. Chauvin and W. Sugimoto, *Electrochem. Commun.*, 2013, **33**, 123–126.
33 B. R. Camacho, C. Morais, M. A. Valenzuela and N. Alonso-Vante, *Catal. Today*, 2013, **202**, 36–43.
34 B. Ruiz-Camacho, M. A. Valenzuela, R. G. Gonzalez-Huerta, K. Suarez-Alcantara, S. E. Canton and F. Pola-Albores, *Int. J. Hydrogen Energy*, 2013, **38**, 12648–12656.
35 S. J. Tauster, S. C. Fung, R. T. K. Baker and J. A. Horsley, *Science*, 1981, **211**, 1121–1125.
36 J. H. Kim, S. Chang and Y. T. Kim, *Appl. Catal., B*, 2014, **158**, 112–118.
37 L. Timperman, A. Lewera, W. Vogel and N. Alonso-Vante, *Electrochem. Commun.*, 2010, **12**, 1772–1775.
38 M. H. Shao, Q. W. Chang, J. P. Dodelet and R. Chenitz, *Chem. Rev.*, 2016, **116**, 3594–3657.
39 S. Sui, X. Y. Wang, X. T. Zhou, Y. H. Su, S. Riffatc and C. J. Liu, *J. Mater. Chem. A*, 2017, **5**, 1808–1825.
40 J. Stacy, Y. N. Regmi, B. Leonard and M. H. Fan, *Renewable Sustainable Energy Rev.*, 2017, **69**, 401–414.
41 C. L. Zhang, X. C. Shen, Y. B. Pan and Z. M. Peng, *Front. Energy*, 2017, **11**, 268–285.
42 M. Escudero-Escribano, K. D. Jensen and A. W. Jensen, *Curr. Opin. Electrochem.*, 2018, **8**, 135–146.
43 M. Kiani, J. Zhang, Y. Luo, C. P. Jiang, J. L. Fan, G. Wang, J. W. Chen and R. L. Wang, *J. Energy Chem.*, 2018, **27**, 1124–1139.
44 Y. Luo and N. Alonso-Vante, *Electrochim. Acta*, 2015, **179**, 108–118.
45 L. Du, Y. Y. Shao, J. M. Sun, G. P. Yin, J. Liu and Y. Wang, *Nano Energy*, 2016, **29**, 314–322.
46 Y. J. Xue, S. S. Sun, Q. Wang, Z. H. Dong and Z. P. Liu, *J. Mater. Chem. A*, 2018, **6**, 10595–10626.
47 M. R. Tarasevich, A. Sadkowski and E. Yeager, in *Comprehensive Treatise of Electrochemistry*, ed. B. Conway, J. M. Bockris, E. Yeager, S. M. Khan and R. White, Springer US, 1983, ch. 6, pp. 301–398.
48 A. Damjanovic, M. A. Genshaw and J. O. Bockris, *J. Chem. Phys.*, 1966, **45**, 4057–4059.
49 V. S. Bagotskii, M. R. Tarasevich and V. Y. Filinovskii, *Sov. Electrochem.*, 1969, **5**, 1158–1161.
50 H. S. Wroblowa, Y. C. Pan and G. Razumney, *J. Electroanal. Chem.*, 1976, **69**, 195–201.
51 A. J. Appleby and M. Savy, *J. Electroanal. Chem.*, 1978, **92**, 15–30.
52 R. W. Zurilla, R. K. Sen and E. Yeager, *J. Electrochem. Soc.*, 1978, **125**, 1103–1109.
53 S. H. Sun, C. B. Murray, D. Weller, L. Folks and A. Moser, *Science*, 2000, **287**, 1989–1992.
54 S. Doniach and M. Sunjic, *J. Phys. C: Solid State Phys.*, 1970, **3**, 285–291.
55 S. Hüfner, *Photoelectron Spectroscopy. Principles and Applications*, Springer Verlag, Berlin, 2003.
56 J. W. Keister, J. E. Rowe, J. J. Kolodziej and T. E. Madey, *J. Vac. Sci. Technol. B*, 2000, **18**, 2174–2178.
57 S. Hüfner, G. K. Wertheim and J. H. Wernick, *Solid State Commun.*, 1975, **17**, 417–422.
58 J. McBreen, W. E. Ogrady, K. I. Pandya, R. W. Hoffman and D. E. Sayers, *Langmuir*, 1987, **3**, 428–433.
59 B. Ravel and M. Newville, *J. Synchrotron Radiat.*, 2005, **12**, 537–541.
60 L. K. Ono, J. R. Croy, H. Heinrich and B. Roldan Cuenya, *J. Phys. Chem. C*, 2011, **115**, 16856–16866.
61 D. R. M. Godoi, H. M. Villullas, F.-C. Zhu, Y.-X. Jiang, S.-G. Sun, J. Guo, L. Sun and R. Chen, *J. Power Sources*, 2016, **311**, 81–90.
62 J. H. Kim, G. Kwon, H. Lim, C. Zhu, H. You and Y. T. Kim, *J. Power Sources*, 2016, **320**, 188–195.
63 J. Masa, C. Batchelor-McAuley, W. Schuhmann and R. G. Compton, *Nano Res.*, 2014, **7**, 71–78.
64 E. Claude, T. Addou, J. M. Latour and P. Aldebert, *J. Appl. Electrochem.*, 1998, **28**, 57–64.
65 M. Lefevre and J. P. Dodelet, *Electrochim. Acta*, 2003, **48**, 2749–2760.
66 N. M. Marković, R. R. Adžić, B. D. Cahan and E. B. Yeager, *J. Electroanal. Chem.*, 1994, **377**, 249–259.
67 J. Perez, H. M. Villullas and E. R. Gonzalez, *J. Electroanal. Chem.*, 1997, **435**, 179–187.
68 U. A. Paulus, T. J. Schmidt, H. A. Gasteiger and R. J. Behm, *J. Electroanal. Chem.*, 2001, **495**, 134–145.
69 S. Mukerjee and J. McBreen, *J. Electrochem. Soc.*, 1999, **146**, 600–606.
70 M. E. Herron, S. E. Doyle, S. Pizzini, K. J. Roberts, J. Robinson, G. Hards and F. C. Walsh, *J. Electroanal. Chem.*, 1992, **324**, 243–258.
71 B. J. Hwang, Y. W. Tsai, J. F. Lee, P. Borthen and H. H. Strehblow, *J. Synchrotron Radiat.*, 2001, **8**, 484–486.
72 E. Antolini, J. R. C. Salgado, M. J. Giz and E. R. Gonzalez, *Int. J. Hydrogen Energy*, 2005, **30**, 1213–1220.
73 A. S. Bandarenka and M. T. M. Koper, *J. Catal.*, 2013, **308**, 11–24.
74 D. T. Sawyer and E. T. Seo, *Inorg. Chem.*, 1977, **16**, 499–501.
75 E. Yeager, *Electrochim. Acta*, 1984, **29**, 1527–1537.
76 M.-H. Shao, P. Liu and R. R. Adzic, *J. Am. Chem. Soc.*, 2006, **128**, 7408–7409.
77 N. Ramaswamy and S. Mukerjee, *Adv. Phys. Chem.*, 2012, 491604, DOI: 10.1155/2012/491604.
78 A. Ignaczak, R. Nazmutdinov, A. Goduljan, L. M. D. Pinto, F. Juarez, P. Quaino, E. Santos and W. Schmickler, *Nano Energy*, 2016, **26**, 558–564.

